Collection 2 VIIRS Reservoir Product Algorithm Theoretical Basis Document (ATBD)

Version 1.0

Shuai Zhang[1], Deep Shah[1], Gang Zhao[1,2], Huilin Gao[1*]

[1] Department of Civil and Environmental Engineering, Texas A&M University

[2] Department of Global Ecology, Carnegie Institution for Science

Contact: hgao@civil.tamu.edu

Table of Contents

1. Introduction

Reservoirs serve as a lifeline in water management (e.g., irrigation, hydropower generation, water supply, and flood control), especially under the ongoing fast population growth and changing climate (Biemans et al., 2011; Cooke et al., 2016; Plate, 2002; Schewe et al., 2014; Veldkamp et al., 2017). Globally, reservoirs supply about 40% of the total irrigation water demand (Biemans et al., 2011) and contribute to more than 60% of renewable energy via hydroelectricity (Murdock et al., 2019). Reservoir storage varies according to natural climate variability as well as the human water use/demand for different sectors (i.e., domestic, agricultural, and industrial). On one hand, near real-time reservoir storage monitoring is essential for mitigating the negative effects of hydro-climatic extremes (droughts and floods) (Mehran et al., 2015; Zhou, 2020). On the other hand, long term records of water retained by global reservoirs can help to evaluate the human impacts on global and regional water cycles (Li et al., 2023; Yigzaw et al., 2018; Zhou et al., 2016). However, because gauge observations for reservoir storage (and/or elevation) are typically not shared, both aforementioned data needs are difficult to satisfy at regional and global scales.

Among the reservoir water budget terms, reservoir evaporation accounts for a substantial amount of the loss of available water—particularly for reservoirs in arid/semi-arid regions (Friedrich et al., 2018). For example, the evaporation volume of Lake Tahoe (located in the western U.S.) represents 40%–60% of the total reservoir output (Friedrich et al., 2018). The annual evaporation rate of Lake Mead is ~1800 mm/year (Moreo, 2015), which greatly exceeds the surrounding evapotranspiration rate (~50 mm/year) (Mu et al., 2011). At a regional scale, the water losses due to evaporation for 200 reservoirs in Texas are equivalent to 20% of their active storage value (Zhang et al., 2017). While only account for 5% of global lake storage capacity, reservoirs contribute 16% to the evaporation volume (Zhao et al., 2022). Thus, it is crucial to incorporate information about reservoir evaporation losses into existing water management practices. Nonetheless, because reservoir evaporation information obtained through reliable in situ measurements (e.g., eddy covariance, energy balance) is hard to acquire, pan evaporation data (which is less accurate due to the lack of consideration of heat storage and fetch effects) have been commonly used as an approximation (Friedrich et al., 2018). For most developing countries, even data about pan evaporation (or its equivalent) are not available.

This is the Algorithm Theoretical Basis Document (ATBD) for the Visible Infrared Imaging Radiometer Suite (VIIRS) Collection 2 Global Water Reservoir (GWR) products from Soumi

NPP (SNPP) and JPSS-1 (also known as NOAA-20) satellites. The GWR product data associated with SNPP and JPSS-1 are named as VNP28 and VJ128, respectively. The reservoir product is available at two temporal resolutions: 8-day (VNP28C2/VJ128C2) and monthly (VNP28C3/VJ128C3). The ATBD for VIIRS is developed by keeping Moderate Resolution Imaging Spectroradiometer (MODIS) ATBD (Zhao et al., 2021) as heritage/reference. It is worth noting that most algorithms for VIIRS and MODIS GWR are similar, however, we improved the VIIRS algorithm in some aspects to mitigate significant uncertainties arising from ice/snow and/or terrain shadows (Shah et al., under review). The objectives of this ATBD are: (1) to give a brief review of the current methods used for monitoring reservoirs using satellite observations; (2) to describe the VIIRS GWR algorithms and the refinements, which are used to generate the product at two temporal resolutions (i.e., 8-day and monthly); (3) to introduce the required input datasets and parameters; (4) to show the validation results for that reservoir area, elevation, storage, and evaporation rate; and (5) to discuss the sources of product uncertainty.

2. Overview and Technical Background

Satellite remote sensing provides an alternative for filling in water reservoir data gaps. Since the 1990s, satellite radar altimeters have been utilized to measure the water levels of large lakes and reservoirs (Birkett, 1995). To date, several databases have been developed to monitor the water levels of inland water bodies at a global scale—including the Global Reservoir and Lake Monitor (G-REALM) (Birkett et al., 2011), the Hydroweb database (Crétaux et al., 2011), and the Database for Hydrological Time Series of Inland Waters (DAHITI) (Schwatke et al., 2015). Meanwhile, the global surface area variations of lakes and reservoirs have been assessed from various satellite instruments, such as the Landsat and MODIS (Donchyts et al., 2016; Khandelwal et al., 2017; Li et al., 2023; Ling et al., 2020; Pekel et al., 2016; Yao et al., 2019; Zhao et al., 2022; Zhao & Gao, 2018). Pekel et al. (2016) developed a Global Surface Water (GSW) dataset using expert system classifiers based on Landsat observations obtained over the last three decades. The more recently published Global Reservoir Surface Area Dataset (GRSAD) provides monthly water area values for over 7000 reservoirs (Zhao & Gao, 2018) which were generated by correcting the underestimations due to cloud contamination in the GSW dataset. Khandelwal et al. (2017) generated 8-day composite water area time series datasets for 94 reservoirs using MODIS multispectral data at 500 m resolution. In the meantime, many studies have focused on generating satellite-based reservoir storage estimations by combining elevation and area observations collected from multiple missions

(Busker et al., 2019; Crétaux et al., 2011; Gao et al., 2012; Zhang et al., 2014). For example, Gao et al. (2012) monitored storage values for 34 global reservoirs from 1992 to 2010 by combining water surface areas from MODIS with water elevations from satellite radar altimetry (which represented 15% of the total global reservoir capacity during that period). The Hydroweb database (http://hydroweb.theia-land.fr/) estimates the storage changes for about 60 large lakes and reservoirs beginning in 1992, using multi-source satellite imagery (e.g., MODIS and Landsat) and radar altimetry data (Crétaux et al., 2011). Busker et al. (2019) analyzed the monthly volume variations between 1984 and 2015 for 137 lakes and reservoirs at a global scale by combining water area values from the GSW dataset (Pekel et al., 2016) and elevation values from DAHITI (Schwatke et al., 2015). The number of lakes with storage estimated has increased to thousands in the recent studies by Li et al. (2023) and Yao et al. (2023).

Meanwhile, some new approaches have been recently developed to estimate evaporation rates and losses from space. For instance, Zhang et al. (2017) estimated the monthly evaporation volumes based on pan-derived evaporative rates and Landsat surface areas for more than 200 reservoirs in Texas. Zhao & Gao (2019) used the Penman Equation (with the heat storage and fetch effects addressed), and generated a first long-term evaporation data record for over 700 reservoirs in the Contiguous United States. Zhao et al. (2020) further improved the calculation of the heat storage change term by leveraging MODIS surface temperature data. Recently, Zhao et al. (2022) developed an evaporation dataset for 1.42 million global lakes. Many other approaches were developed and tested at individual locations (Althoff et al., 2019; Meng et al., 2020; Mhawej et al., 2020).

Despite the development of remotely sensed reservoir datasets, consistent, comprehensive, long-term, and operationally monitored reservoir products are still lacking at the global scale. Therefore, we developed the National Aeronautics and Space Administration (NASA)'s long-term standard GWR product suite from moderate-resolution remote sensing data such as the MODIS and VIIRS. Given the forthcoming end-of-life plans for the MODIS platforms, the issue of GWR continuity requires greater attention. Therefore, the newly developed VIIRS GWR (VNP28/VJ128) can serve as a viable successor to MODIS observations for ensuring long-term GWR continuity. More details regarding the MODIS and VIIRS GWR product continuity is described in Shah et al. (under review).

3. VNP28/VJ128 Algorithm Descriptions

The VNP28C2/VJ128C2 product includes the reservoir area, elevation, and storage results at 8-day temporal resolution. Figure 1 shows the flowchart for generating the C2 (8-day) product. The algorithms corresponding to both products are explained in the following sections. First, the 8-day reservoir area values were extracted from the 500-m Near Infrared (NIR) band of VIIRS surface reflectance (VNP09H1/VJ109H1) data. Then, the area values were applied to the Area-Elevation (A-E) relationship for the given reservoir provided by the GRBD (Li et al., 2020) to calculate the corresponding elevation values. Lastly, the reservoir storage can be estimated after Gao et al. (2012).

Figure 1. Flow chart of the algorithm for deriving the VNP28C2/VJ128C2 product, which contains 8-day area, elevation, and storage results for the 164 reservoirs. The product components are shown in green boxes.

The VNP28C3/VJ128C3 product includes the evaporation rate and volumetric evaporation loss in addition to the area, elevation, and storage results at monthly temporal resolution. Figure 2 shows the flowchart for generating the VNP28C3/VJ128C3 monthly product. The monthly area values were first estimated based on the composite of the 8-day area classifications, and then converted to monthly elevation and storage results using the A-E relationship (Figure 2). In addition, monthly evaporation rates were estimated after the Lake Temperature and Evaporation Model (LTEM, Zhao et al., 2020) using VIIRS Land Surface Temperature (LST) product (VNP21A2/VJ121A2) and meteorological data from the Global Land Data Assimilation System (GLDAS) (Rodell et al., 2004). Lastly, the monthly evaporative volumetric losses were calculated as the product of evaporation rate and reservoir open water area values.

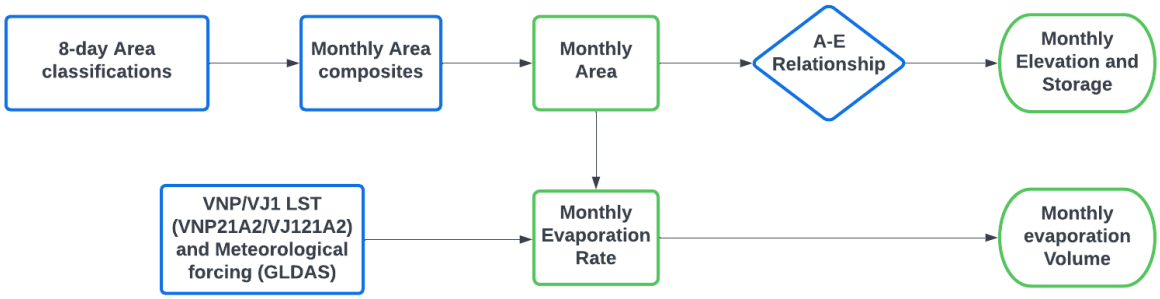

Figure 2. Flow chart of the algorithm for deriving the VNP28C3/VJ128C3 product, which contains monthly area, elevation, storage, evaporation rate, and volumetric evaporation loss results for the 164 reservoirs. The product components are shown in green boxes.

The detailed algorithms for generating reservoir area, elevation, storage, evaporation rate, and evaporation volume are explained in the following subsections.

3.1 Algorithms for reservoir area

3.1.1 Algorithm for VNP28C2/VJ128C2 (8-day product)

The algorithm for estimation of reservoir area has been explained in detail in MODIS ATBD (Zhao et al., 2021). Here, we explain the VIIRS area algorithm with an example of Lake Hawea in New Zealand (Figure 3). To ensure comprehensive coverage of the water extent, we initially buffered the reservoir shapefile (obtained from HydroLAKES; Messager et al., 2016) by 1 km outward. The classification and enhancement operations were performed within this buffered area. For each 8-day period, we selected the VNP09H1/VJ109H1 NIR image that overlapped with the reservoir shapefile (Figure 3a). Subsequently, pixels affected by clouds, cloud shadows, and snow/ice (identified using the Quality Assurance (QA) band of VNP09H1/VJ109H1) were labeled as 'No Data', denoting contaminated pixels. Next, the Otsu thresholding method (Otsu, 1979) was applied to obtain the raw water area classification (Figure 3b). However, it is evident that this raw classification underestimates the actual water area due to various above-mentioned contaminations. To address this issue, we utilized the enhancement algorithm developed by Zhao et al. (2020) to correct the underestimation (Figure 3c). This enhancement algorithm incorporates edge detection techniques and water occurrence images provided by the Global Surface Water (GSW) dataset (Pekel et al., 2016) to correct the raw classification. Further details regarding the enhancement algorithm can be found in Zhao et al. (2020).

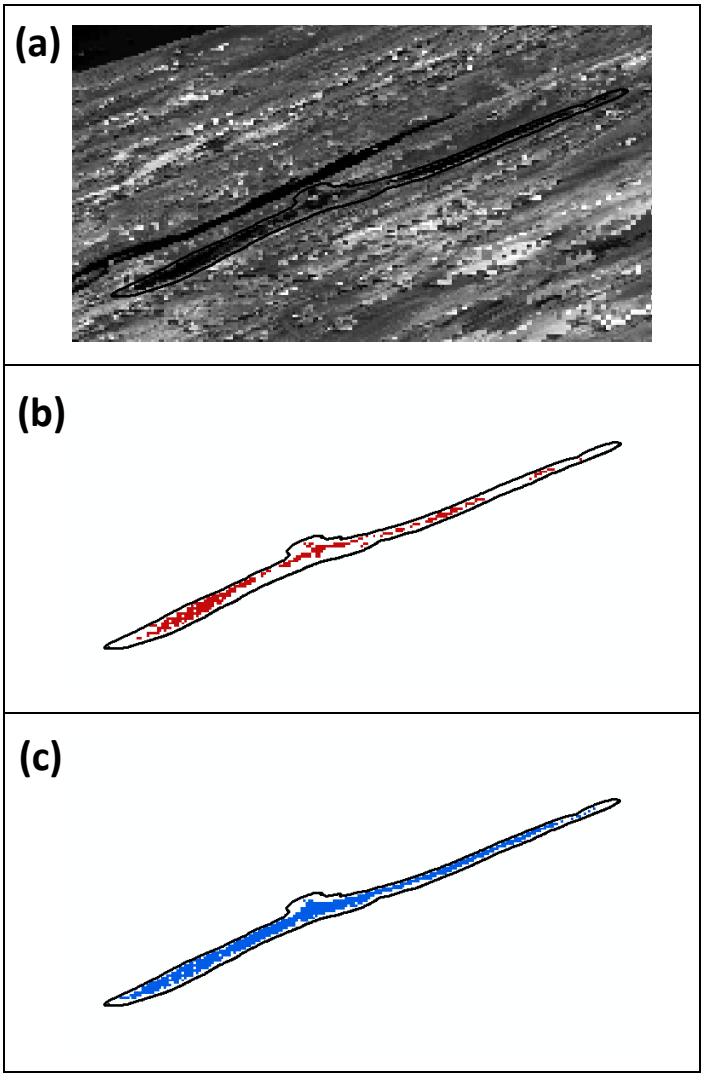

Figure 3. The VNP image collected on day 347 of 2021 over Lake Hawea (ID 131), New Zealand. (a) The original reflectance image; (b) the raw water from Otsu classification; (c) the improved water extraction by enhancement operation.

As compared to MODIS algorithms, the following improvements have been made with in the VIIRS 8-day area estimations: 1) Adding contamination percentage values to the 8-day and monthly area outputs; 2) Improving the enhancement algorithm using an edge detection approach; and 3) Adopting the 8-day terrain shadow masks to improve the classification results.

To improve the data quality assessment for users, we have incorporated contamination percentage values (pertaining to cloud, cloud shadow, and snow/ice) into both the 8-day and monthly area products. These values are obtained from the composite QA bands which are newly added to the 8-day classification images (i.e., VNP28A2/VJ128A2). These QA bands have combined the QA information from the reflectance product (e.g., VNP09H1/VJ109H1)

with the newly introduced fields related to classification results (i.e., raw water, enhanced water, and not-water). Although the composite QA bands are not publicly released since they are intermediate products, the contamination percentage values are made available to the public through the VNP28C2/VJ128C2 and VNP28C3/VJ128C3 products. This enables users to comprehensively understand the data quality associated with the GWR VIIRS product.

The current MODIS product incorporates an enhancement algorithm developed by Zhang et al. (2014), whereas the VIIRS product utilizes an enhancement algorithm developed by Zhao et al. (2020). While the enhancement algorithm employed in the current MODIS version generally performs well for most reservoirs, it exhibits relatively larger uncertainties when applied to reservoirs located in high latitude regions (Li et al., 2021). One challenge lies in using a threshold to correct misclassification in both enhancement algorithms. This threshold is estimated using percentile values derived from the edge pixels of a reservoir. Unlike MODIS, the VIIRS enhancement algorithm is based on physical principles and is not dependent on specific parameters. This characteristic enhances its capability to handle edge pixels in high-latitude regions, improving performance (Zhao et al., 2020). For a detailed explanation regarding algorithm changes, please refer to Zhao et al. (2020). Overall, the VIIRS enhancement algorithm demonstrates enhanced stability on a global scale.

In order to mitigate area classification errors in reservoirs surrounded by complex and steep terrain, a series of 8-day terrain shadow masks were generated to represent climatological conditions (Figure 4). For example, Figure 4 depicts the climatology of the terrain shadow area within Lake Hawea. The generation of these masks followed the approach developed by Leidman et al., (2021), which we have further improved upon by incorporating the average 8-day zenith solar angle during satellite overpass and the Shuttle Radar Topography Mission (SRTM) Digital Elevation Model (DEM). Initially, the masks were created at a 30-meter resolution and aggregated to match the VNP09H1/VJ109H1 resolution. To implement this algorithm refinement, minor modifications were made to the 8-day image classification code, ensuring that pixels falling within the shadow mask areas were not utilized for raw classification. These modifications were implemented to achieve more accurate raw classifications and improve the representation of water surface areas, aspects that were not adequately addressed in the MODIS product. Consequently, the VIIRS GWR algorithms exhibit greater precision compared to MODIS.

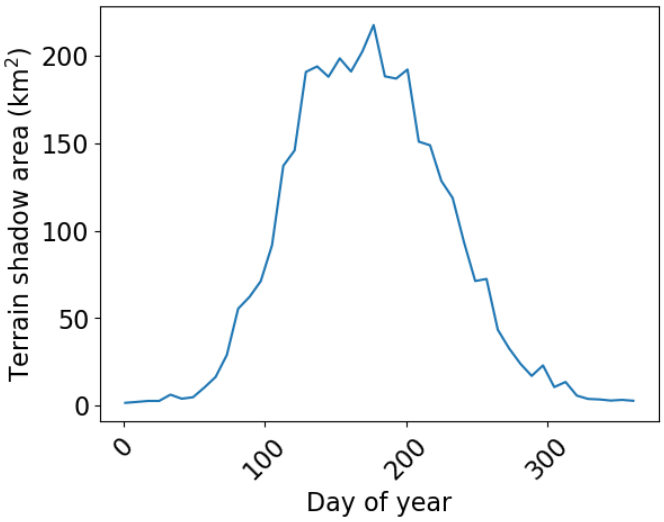

Figure 4. The climatology of terrain shadow area within Lake Hawea (ID 131).

3.1.2 Algorithm for VNP28C3 (monthly product)

The monthly enhanced area values were estimated similarly as 8-day product but based on the composite of the 8-day area classifications. A pixel was assigned as a water pixel if this pixel was classified as water in any of the 8-day images within this month. This "max" composite approach might slightly overestimate the monthly mean water area value. However, given that the water area variation within a month is relatively small for large reservoirs (except when there is flooding), the monthly area time series can adequately represent the long-term dynamics of the reservoir.

3.2 Algorithms for reservoir elevation and storage

The enhanced area values (A_{VIIRS}) were applied to the Area-Elevation (A-E) relationship (Equation (1)) to calculate the corresponding elevation values (h_{VIIRS}). For each given reservoir, the A-E relationship function, $f()$, was adopted from the Global Reservoir Bathymetry Dataset (GRBD; Li et al. (2020)).

$$h_{VIIRS} = f(A_{VIIRS}) \quad (1)$$

The corresponding reservoir storage can be estimated using Equation (2) (after Gao et al. (2012)):

$$V_{VIIRS} = V_c - (A_c + A_{VIIRS})(h_c - h_{VIIRS})/2 \quad (2)$$

where V_c, A_c, and h_c represent storage, area, and water elevation values at capacity (see appendix A); and V_{VIIRS}, A_{VIIRS}, and h_{VIIRS} are the estimated storage, area, and water elevation from VIIRS.

3.3 Algorithms for evaporation rate and volume

3.3.1 Calculating evaporation rate

We employed the LTEM to estimate monthly evaporation rates, which incorporates the Penman equation while accounting for heat storage and fetch effects. To drive the LTEM model, we obtained the 8-day day/night land surface temperature (LST) data and meteorological forcing data from the GLDAS. The detailed algorithm for estimating the evaporation rate (for VNP28C3/VJ128C3) is same as explained in MODIS ATBD (Zhao et al., 2021). To get more detailed information about evaporation estimation, please refer to Zhao et al. (2020) and (2021).

3.3.2 Calculating volumetric evaporation

After calculating the evaporation rate time series, the volumetric evaporation can be inferred as a function of the evaporation rate and reservoir area. In the case of MODIS version (i.e., MOD28C3), the evaporation volume was calculated by multiplying the evaporation rate with the enhanced surface area. However, in high-latitude regions, the enhanced surface area may include both open water and ice-covered areas. As the evaporation loss is negligible for the ice-covered portion, for VIIRS, we improved the estimation of evaporation volume by multiplying the evaporation rate with only the fraction of the open water area (Equation 3). The composite QA band, as described earlier, was used to distinguish between open-water pixels and those covered by ice.

$$V_E = E \times A \tag{3}$$

Where V_E is volumetric evaporation, E is the evaporation rate (mm/d) and A is the open water area (km^2).

4. Input Datasets

The input datasets include three categories: reservoir shapefiles, input variables, and reservoir parameters. The details of these inputs can be found in the following sub-sections.

4.1 Reservoir shapefiles

The reservoir shapefiles were adopted from HydroLAKES (Messager et al., 2016) and OpenStreetMap (Haklay & Weber, 2008). For a given reservoir, the two shapefiles were compared and the one with the larger area was selected. By leveraging these two shapefile datasets, the possible underestimations from either of them can be eliminated. It should be noted that we manually corrected some polygons that were found to have large discrepancies from Google maps. The purposes of the shapefiles are two-fold: for extracting the meteorological data over the reservoirs and for generating reservoir masks.

4.2 Input variables

The time varying input variables are from other VIIRS products and meteorological data, which are summarized in Table 1.

Table 1. Summary of the input variable names, sources and purposes used in this study. The land surface temperature contains day/night surface temperature for inland water areas.

Data	Spatial resolution	Temporal resolution	Purpose	Reference
VIIRS surface reflectance (VNP09H1/VJ109H1)	500 m	8-day	Water area extraction	Vermote et al., 2016
VIIRS LST (VNP21A2/VJ121A2)	1 km	8-day	WST extraction	Hulley & Hook, 2018
GLDAS-2.1	0.25°	1-month	Meteorological forcing data for LTEM	Beaudoing & Rodell, 2020; Rodell et al., 2004

(1) Inputs from other VIIRS products

For VNP28C2, the 8-day surface reflectance (VNP09H1; Vermote et al., 2016) data were collected for water area extraction. Specially, only the near-infrared (NIR) band was used due to its high spatial resolution (i.e., 500 m for VIIRS). The NIR band has been commonly utilized

for the extraction of water bodies because it is strongly absorbed by water but scarcely absorbed by terrestrial dry soil and vegetation (McFeeters, 1996). The A-E relationships were adopted from GRBD (Li et al., 2020), which have proven to be of high quality through validation against in situ data. Then, the 8-day water area estimations were applied to the A-E relationships to derive elevation and storage values. Moreover, we used the 8-day day/night land surface temperature (LST) products (VNP21A2; Hulley & Hook, 2018) and Global Land Data Assimilation System (GLDAS; Rodell et al., 2004) meteorological forcing data to estimate the evaporation rates and volumes.

(2) Meteorological data

We obtained the meteorological data from the NASA GLDAS Version 2.1 (GLDAS-2.1; Rodell et al., 2004; Beaudoing and Rodell, 2020) to drive the LTEM. In this version GLDAS is forced with a combination of model and observation data from 2012 to present. For instance, it was forced with National Oceanic and Atmospheric Administration (NOAA)/Global Data Assimilation System (GDAS) atmospheric analysis fields (Derber et al., 1991), the disaggregated Global Precipitation Climatology Project (GPCP) precipitation fields (Adler et al., 2003), and the Air Force Weather Agency's AGRicultural METeorological modeling system (AGRMET) radiation fields which became available for March 1, 2001 onwards. We used monthly downward shortwave radiation (W/m^2), air temperature (in K), specific humidity (in kg/kg), and wind speed (in m/s) data from 2012 to present, with a spatial resolution of 0.25 degree to drive the LTEM. For any reservoir covering multiple GLDAS grids, the meteorological forcings were first averaged over those grids.

4.3 Reservoir parameters

The following reservoir parameters are used for generating the products: storage at capacity, elevation at capacity, surface area at capacity, A-E relationship, average reservoir depth, and average latitude. Detailed information for each reservoir is provided in appendix A. More details about the algorithms for generating the A-E relationships are available in Li et al. (2020).

5. Results and Uncertainties

5.1 Validation results

5.1.1 Comparing VIIRS water surface areas with MODIS and Landsat measurements

Since elevation and storage are estimated by applying A-E relationships on the surface area, it is crucial to first evaluate the reservoir surface area. The long-term records of the in-situ reservoir area are still lacking on a global scale. Therefore, we compared the monthly VIIRS surface area (VNP28C3/VJ128C3) with MODIS (MOD28C3) and Landsat-based Global Reservoir Surface Area Dataset (GRSAD; Zhao and Gao, 2018) during their overlapping periods (2012-2021 for MODIS and 2012-2018 for Landsat). The GRSAD dataset was developed after correcting the water area underestimation of the GSW dataset caused by both cloud/shadow/ice contamination and the Landsat-7 scan line corrector failure.

We find VIIRS based surface area shows good agreement with the MODIS-based surface area with an R^2 value of 0.99. The Relative Bias (RB) between the VNP and MOD as well as between VJ1 and MOD were found to be around -5% (Figure 5). The negative bias represents a slight underestimation of the VIIRS area as compared to the MODIS. This underestimation can be attributed to differences in the sensors (different resolutions) and algorithms generating surface area. The VIIRS-based product uses a different classification algorithm than MODIS and accounts for the terrain shadow effect that the MODIS-based product does not. The exclusion of the terrain shadow effect in the algorithm could overestimate the surface area in the lakes located in the mountainous region.

We also find good agreement between VIIRS and Landsat-based surface area, with an R^2 value of 0.99 and RB value of 1.97% (Figure 5). Most of the points centered on the regression line (slope=1.01); however, there are a few disagreements. This could be because the collection dates and methods to derive the monthly area from Landsat and VIIRS differ. It could also be due to the relatively low spatial resolution of VIIRS, which makes it more susceptible to mixed pixels in relatively small reservoirs (Li et al., 2021) Overall, the VIIRS-based area exhibits satisfactory consistency with other satellite datasets.

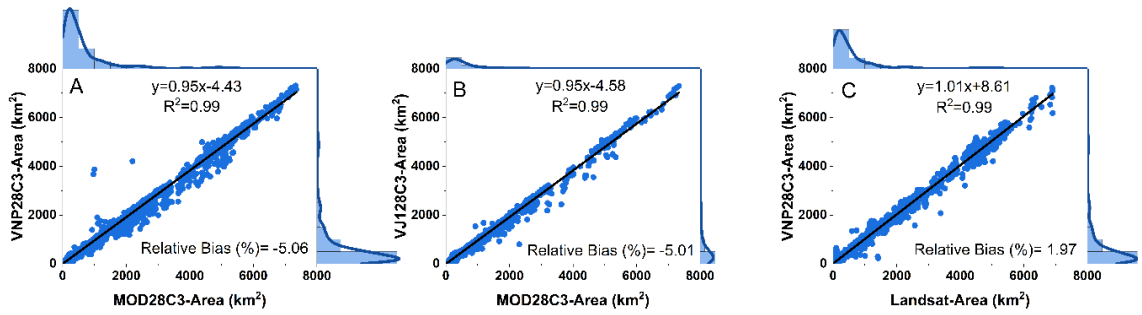

Figure 5. The evaluation of the monthly VIIRS reservoir surface area. (A) The comparison of the monthly area estimations between MODIS (Terra) and VIIRS (SNPP) from 2012 to 2021

for the 164 reservoirs, (B) same as (A) but for JPSS-1 from March 2020 to December 2021, (C) same as (A) but between VIIRS (SNPP) and Landsat from 2012-2018. Lake Baikal is excluded from the figure and analysis due to its extremely large values.

5.1.2. Evaluation of the VIIRS elevation and storage products

We evaluated the remotely sensed elevation and storage from VIIRS with MODIS and the in-situ observations at twelve Indian reservoirs, for which the daily and monthly in-situ data were obtained from the Indian Central Water Commission (CWC: http://cwc.gov.in/, accessed on 2nd May 2022) between 2012 and 2021. To validate the 8-day product, we considered the daily in-situ observation of the same date as VIIRS. For the evaluation of the monthly product, we used monthly averaged in-situ observations from CWC. We selected the Indian reservoirs for validation purposes due to their large variability, which can better evaluate the efficiency of our algorithm.

Figures 6 and 7 show the 8-day elevation and storage validation results. We find good consistency of VIIRS (VNP28C2) elevation with in-situ observations, with an average R^2 value of 0.77, an average RMSE value of 3.34m, and an average NRMSE value of 13.53% (Figure 6). While elevation exhibits good consistency at most locations, we noticed cases of overestimation (i.e., Tungabhadra) and underestimation (e.g., Yeleru, Nagarjuna). These over and underestimations could be due to mixed pixels at the reservoir edge and uncertainties in the A-E relationship (coefficients). Moreover, we observed that VIIRS elevation was in good agreement with MODIS (MOD28C2), which can serve as a basis to establish the continuity of MODIS products with VIIRS products. Similar to elevation, the in-situ storage variation was satisfactorily captured by VIIRS, with an average R^2 value of 0.84, an average RMSE value of 0.47 km3, and an average NRMSE value of 16.45% (Figure 7). Jayakwadi reservoir showed a maximum R^2 value of 0.95, and Nagarjuna reservoir showed the least R^2 value of 0.76. With respect to the continuity perspective, we recognized substantial agreement between MODIS and VIIRS storage estimates.

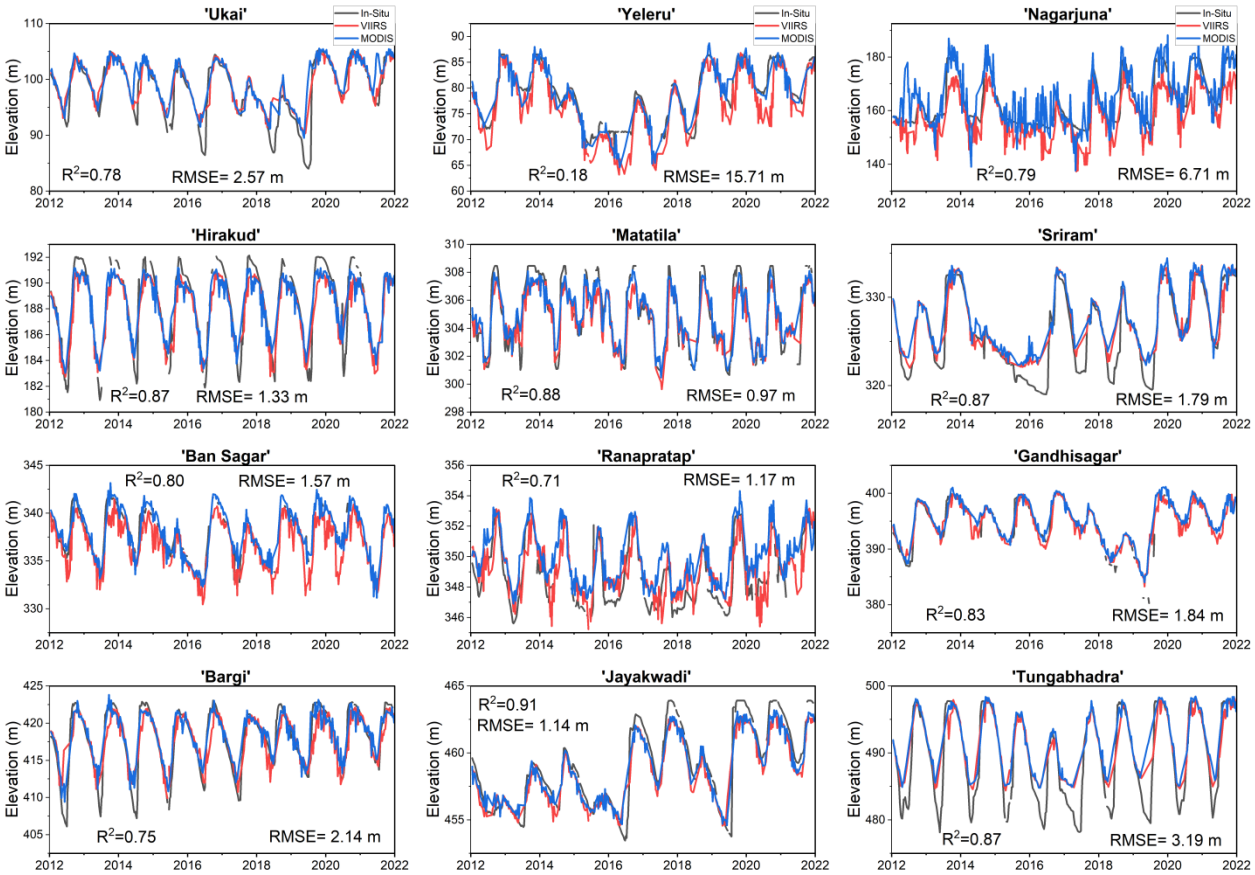

Figure 6. Validation of VIIRS (VNP28C2) 8-day elevation (red) against the in-situ (black) and MODIS (MOD28C2) elevation (blue) observations for twelve Indian reservoirs from 2012 to 2021.

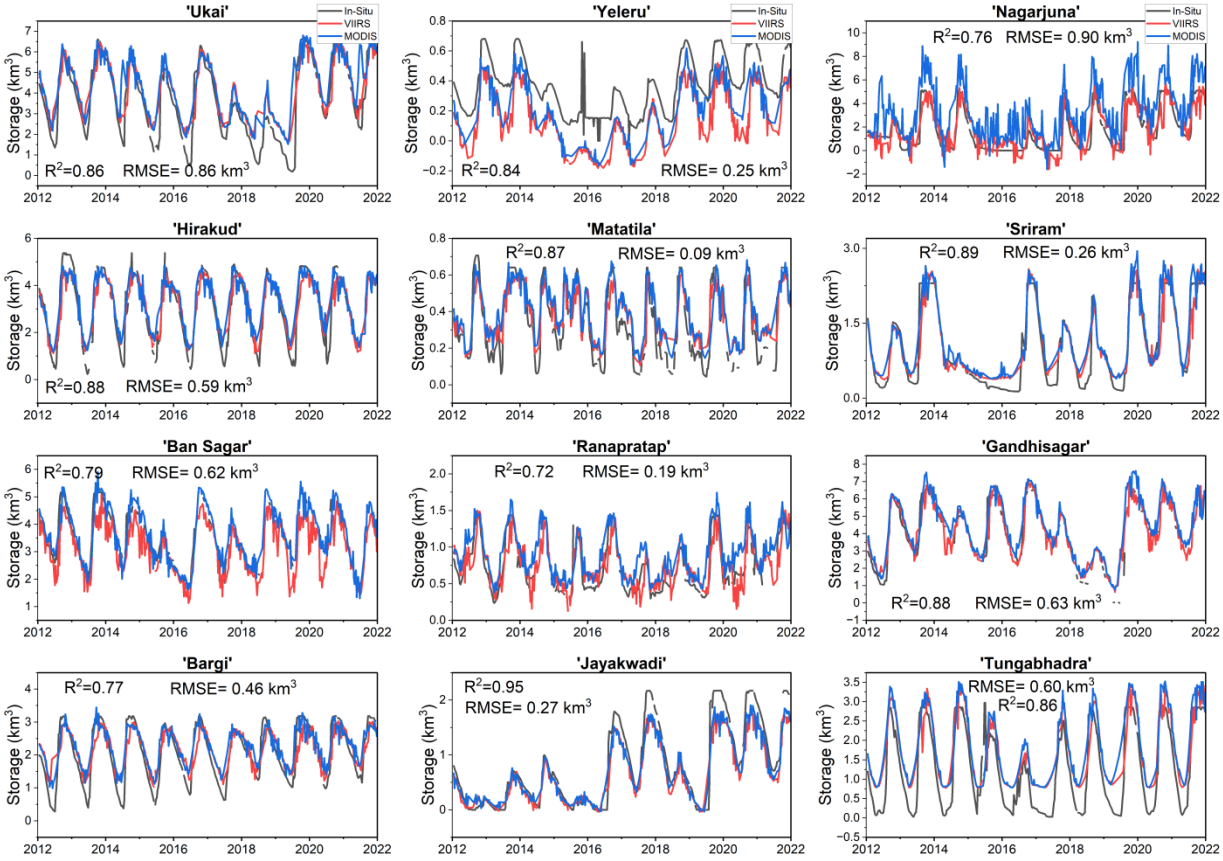

Figure 7. Validation of VIIRS (VNP28C2) 8-day storage (red) against the in-situ (black) and MODIS (MOD28C2) storage (blue) observations for twelve Indian reservoirs from 2012 to 2021.

In a similar fashion, we validated the monthly VIIRS (VNP28C3) elevation and storage with the in-situ and MODIS (MOD28C3) observations. Since the monthly data is generated from the composite of 8-day data, they also manifest robust consistency as 8-day data (Figures 8 and 9). VIIRS monthly reservoir area values were generated from the composited results of three or four 8-day area images from VNP28C2, reducing the adverse effects of cloud contamination at the 8-day time step and making them smoother. Regarding elevation, the VIIRS results show good agreement against the in-situ data with an average R^2 value of 0.75, an average RMSE value of 2.59 m, and an average NRMSE value of 14.25% (Figure 8). As for storage, the validation results were also satisfactory, with an average R^2 value of 0.80, an average RMSE value of 0.50 km^3, and an average NRMSE value of 17.54% (Figure 9). The consistency between VIIRS and MODIS was also exceptional, highlighting that VIIRS-based reservoir products can replace MODIS-based reservoir products after the decommissioning of MODIS.

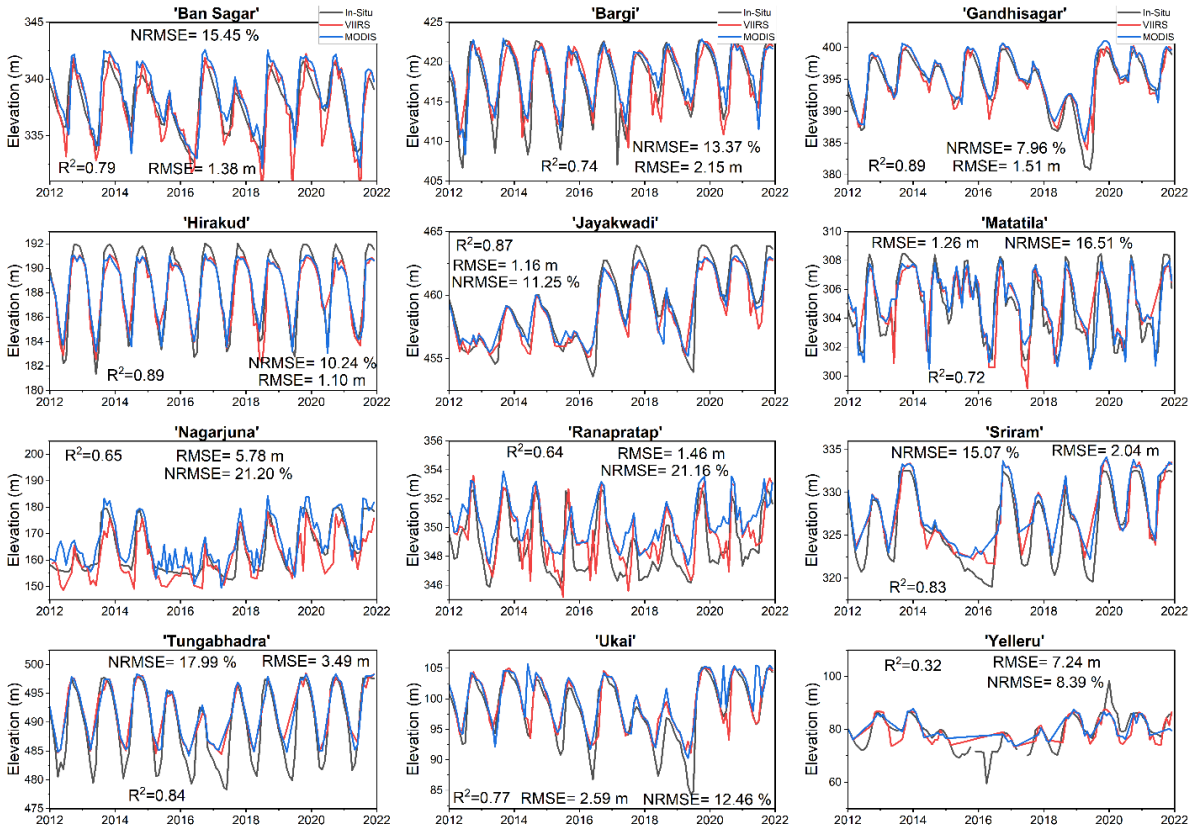

Figure 8. Validation of VIIRS (VNP28C3) monthly elevation (red) against the in-situ (black) and MODIS (MOD28C3, blue) observations for twelve Indian reservoirs from 2012 to 2021.

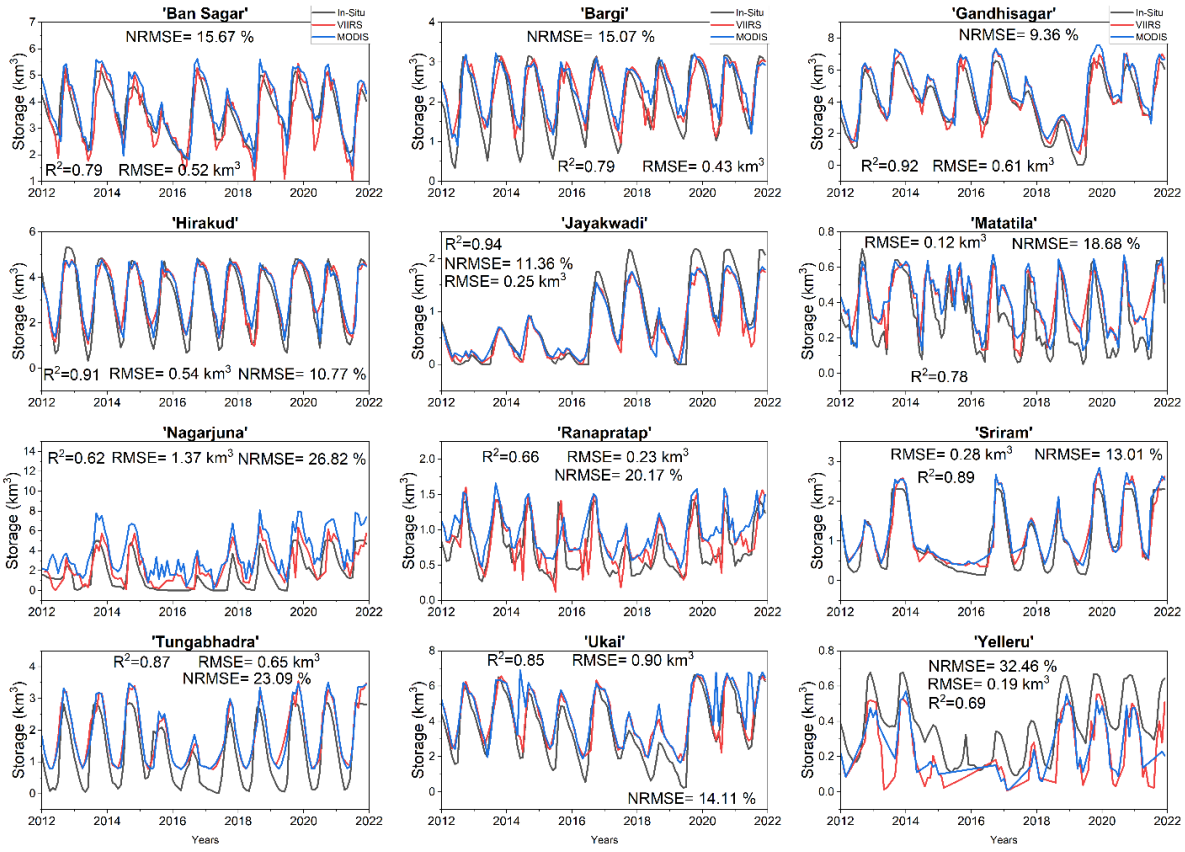

Figure 9. Validation of VIIRS (VNP28C3) monthly storage (red) against the in-situ (black) and MODIS (MOD28C3, blue) observations for twelve Indian reservoirs from 2012 to 2021.

5.1.3. Validating the evaporation rate product against in situ observations

We tested the VIIRS (VNP28C3) evaporation rate against the in-situ and MODIS (MOD28C3) evaporation rates at Lake Mead and Lake Powell in North America. The validation of the evaporation rate was limited by the availability of high-quality in-situ data, which highlights the importance of generating our operational reservoir evaporation data product at a global scale. We obtained the eddy covariance (EC) evaporation rate measurements for Lake Mead between 2012 and 2015 from the United States Geological Survey (USGS; Moreo, 2015) and for Lake Powell between November 2018 and December 2021 from the Bureau of Reclamation (BoR; Holman et al., 2022).

VIIRS captured the seasonality of the evaporation rate at both locations. At Lake Mead, the VIIRS evaporation rate showed good agreement with in-situ measurements with R^2 value of 0.75, RMSE value of 1.07mm/day, and NRMSE value of 18.7% (Figure 10). The evaporation rate from VIIRS at Lake Mead also offers good consistency with MODIS. However, at Lake Powell, we found low agreement of VIIRS evaporation rate with the in-situ data with R^2

value of 0.37, RMSE value of 1.58 mm/day, and NRMSE value of 37.58% (Figure 10). This can be attributed to differences in the method used to obtain the evaporation rate. While in-situ data were measured using the eddy covariance method, the VIIRS evaporation rate was estimated using the LTEM model that accounts for a heat storage effect. Although this can lead to bias in absolute values of evaporation rates, the overall seasonality was well captured in both cases.

Similar to other variables, MODIS and VIIRS evaporation rate estimates show good consistency (Figure 10). The slight differences in MODIS and VIIRS-based evaporation rate values could be due to differences in sensors and LST products used in LTEM. Zhao et al. 2020 validated the MODIS evaporation rate or water temperature profiles at eleven locations located in different climates, which cover a good range of sizes, depths, and elevations, and thus are representative for testing the robustness of LTEM. They found a satisfactory performance of MODIS-based evaporation rate against the in-situ observations. As most of those in-situ data were unavailable after 2012 (after the launch of VIIRS), we could not validate the VIIRS evaporation rate at more locations. However, since MODIS and VIIRS show good consistency for the overlapping period, we anticipate that the VIIRS evaporation rate should be able to offer substantial agreement at other locations.

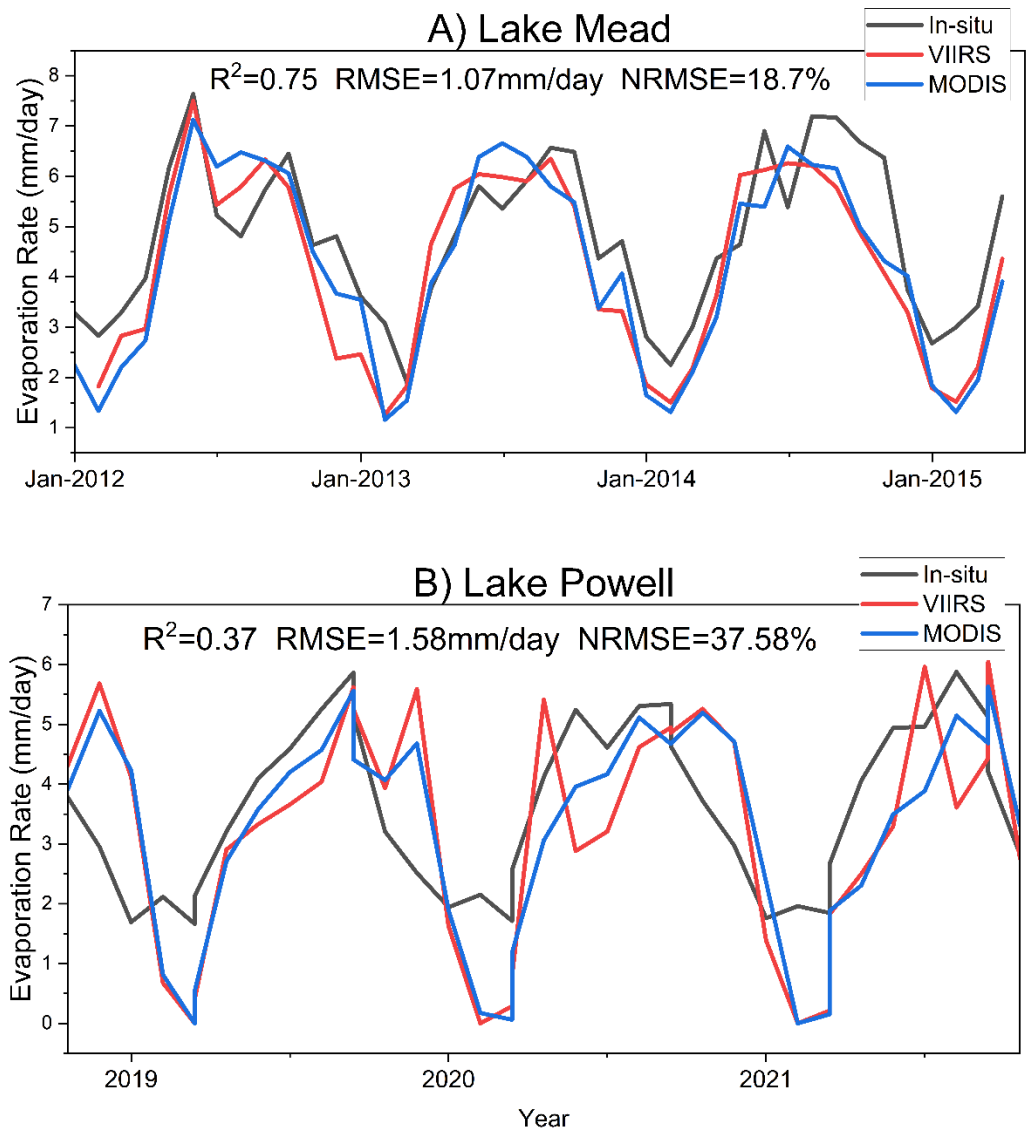

Figure 10. Comparison of the VIIRS (VNP28C3) evaporation rates (red) against the in-situ data (black) and MODIS (MOD28C3) observations (blue) at (A) Lake Mead and (B) Lake Powell. In-situ data were measured using eddy covariance (EC) measurements for Lake Mead from 2012 to 2015 and for Lake Powell from November 2018 to December 2021.

4.2 Sources of uncertainties

The sources of uncertainty with regard to the VIIRS reservoir surface area are associated with both the raw image classification using the VIIRS reflectance product, and the classification enhancement algorithm. The accuracy of the Otsu classification of the VIIRS NIR images is affected by the mixed pixels (i.e., partially covered by water and partially covered by land) at the reservoir boundaries, terrain shadow pixels, as well as by ice over the lakes. The reliability of the enhancement algorithm depends on the data quality of both the water occurrence image and the raw water classification. In high latitude regions, the water occurrence image generally

shows small surface area dynamics (i.e., the distribution of occurrence values highly skewed to the left). Thus, the pixels with low occurrence values have relatively large uncertainties. The accuracy of classification is heavily influenced by confounding pixels, such as clouds, snow/ice, and terrain shadows, therefore, the contamination percentage value provided in the product serve can serve as a director indicator of uncertainty.

The reservoir elevation and storage estimation uncertainties include reservoir surface area uncertainties (see above), A-E relationship uncertainties, and the reservoir configuration uncertainties. According to Equation (2), the estimated storage will be biased if the characteristics at capacity (storage, area, and elevation) are not accurate. Even when these factors have been correctly documented, the storage capacity may have changed due to sedimentation over time. Since the reservoir elevations are inferred only from areas and A-E relationships, they are not affected by reservoir configuration uncertainties.

Sources of evaporation rate uncertainty mainly include forcing data uncertainty and model structure/parameter uncertainty. Specifically, the forcing data used in this study (i.e. GLADS-2) is a land-based meteorological record. Although the increased humidity on the lake surface is represented by the wind function (McJannet et al., 2012; Zhao & Gao, 2019), differences in the wind speeds between lake and land regions are ignored—which might introduce some uncertainties (Schwab & Morton, 1984). In addition, the LTEM and its parameters can also produce uncertainties. For example, the formulation of the light attenuation coefficient (λ_PAR) is simplified in Zhao et al. (2020). However, λ_PAR is affected by suspended solids, phytoplankton concentration level, and spectral distribution of solar radiation, and thus is constantly changing (Lee et al., 2005; Pinhassi et al., 2016).

The reservoir volumetric evaporation uncertainties can be attributed to evaporation rate and surface area uncertainties, which have been discussed above.

6. References

Adler, R. F., Huffman, G. J., Chang, A., Ferraro, R., Xie, P. P., Janowiak, J., Rudolf, B., Schneider, U., Curtis, S., Bolvin, D., Gruber, A., Susskind, J., Arkin, P., & Nelkin, E. (2003). The version-2 global precipitation climatology project (GPCP) monthly precipitation analysis (1979-present). *Journal of Hydrometeorology*, *4*(6). https://doi.org/10.1175/1525-7541(2003)004<1147:TVGPCP>2.0.CO;2

Althoff, D., Rodrigues, L. N., & Silva, D. D. da. (2019). Evaluating evaporation methods for estimating small reservoir water surface evaporation in the Brazilian savannah. *Water (Switzerland)*, *11*(9). https://doi.org/10.3390/w11091942

Beaudoing, H., & Rodell, M. (2020). *GLDAS Noah Land Surface Model L4 monthly 0.25 x 0.25 degree V2.1.* . Greenbelt, Maryland, USA, Goddard Earth Sciences Data and Information Services Center (GES DISC).

Biemans, H., Haddeland, I., Kabat, P., Ludwig, F., Hutjes, R. W. A., Heinke, J., Von Bloh, W., & Gerten, D. (2011). Impact of reservoirs on river discharge and irrigation water supply during the 20th century. *Water Resources Research*, *47*(3). https://doi.org/10.1029/2009WR008929

Birkett, C. M. (1995). The contribution of TOPEX/POSEIDON to the global monitoring of climatically sensitive lakes. *Journal of Geophysical Research*, *100*(C12). https://doi.org/10.1029/95jc02125

Birkett, C., Reynolds, C., Beckley, B., & Doorn, B. (2011). From research to operations: The USDA global reservoir and lake monitor. In *Coastal Altimetry*. https://doi.org/10.1007/978-3-642-12796-0_2

Busker, T., De Roo, A., Gelati, E., Schwatke, C., Adamovic, M., Bisselink, B., Pekel, J. F., & Cottam, A. (2019). A global lake and reservoir volume analysis using a surface water dataset and satellite altimetry. *Hydrology and Earth System Sciences*, *23*(2). https://doi.org/10.5194/hess-23-669-2019

Cooke, D. G., Welch, E. B., Peterson, S. A., & Nichols, S. A. (2016). Restoration and Management of Lakes and Reservoirs. In *Regulated Rivers: Research & Management* (Issue 2).

Crétaux, J.-F., Arsen, A., Calmant, S., Kouraev, A., Vuglinski, V., Bergé-Nguyen, M., Gennero, M.-C., Nino, F., Abarca Del Rio, R., Cazenave, A., & Maisongrande, P. (2011). SOLS: A lake database to monitor in the Near Real Time water level and storage variations from remote sensing data. *Advances in Space Research*, *47*(9), 1497–1507. https://doi.org/https://doi.org/10.1016/j.asr.2011.01.004

Derber, J. C., Parrish, D. F., & Lord, S. J. (1991). The New Global Operational Analysis System at the National Meteorological Center. *Weather and Forecasting*, *6*(4), 538–547. https://doi.org/https://doi.org/10.1175/1520-0434(1991)006<0538:TNGOAS>2.0.CO;2

Donchyts, G., Baart, F., Winsemius, H., Gorelick, N., Kwadijk, J., & van de Giesen, N. (2016). Earth's surface water change over the past 30 years. *Nature Climate Change*, *6*(9), 810–813. https://doi.org/10.1038/nclimate3111

Friedrich, K., Grossman, R. L., Huntington, J., Blanken, P. D., Lenters, J., Holman, K. D., Gochis, D., Livneh, B., Prairie, J., Skeie, E., Healey, N. C., Dahm, K., Pearson, C., Finnessey, T., Hook, S. J., & Kowalski, T. (2018). Reservoir Evaporation in the Western United States: Current Science, Challenges, and Future Needs. *Bulletin of the American Meteorological Society*, *99*(1). https://doi.org/10.1175/bams-d-15-00224.1

Gao, H., Birkett, C., & Lettenmaier, D. P. (2012). Global monitoring of large reservoir storage from satellite remote sensing. *Water Resources Research*, *48*(9). https://doi.org/10.1029/2012WR012063

Haklay, M., & Weber, P. (2008). OpenStreetMap: User-Generated Street Maps. Pervasive Computing. *IEEE Pervasive Computing*, *7*(4).

Holman, K., P. C., J. R., H. J. L., & V. J. (2022). *Evaporation from Lake Powell. In-situ Monitoring between 2018 and 2021 [Dataset]*.

Hulley, G., & Hook, S. (2018). *VIIRS/NPP Land Surface Temperature and Emissivity 8-Day L3 Global 1km SIN Grid V001 [Data set]*. NASA EOSDIS Land Processes DAAC.

Khandelwal, A., Karpatne, A., Marlier, M. E., Kim, J., Lettenmaier, D. P., & Kumar, V. (2017). An approach for global monitoring of surface water extent variations in reservoirs using MODIS data. *Remote Sensing of Environment*, *202*. https://doi.org/10.1016/j.rse.2017.05.039

Lee, Z.-P., Darecki, M., Carder, K. L., Davis, C. O., Stramski, D., & Rhea, W. J. (2005). Diffuse attenuation coefficient of downwelling irradiance: An evaluation of remote sensing methods. *Journal of Geophysical Research: Oceans*, *110*(C2). https://doi.org/https://doi.org/10.1029/2004JC002573

Leidman, Sasha. Z., Rennermalm, Å. K., Lathrop, R. G., & Cooper, Matthew. G. (2021). Terrain-Based Shadow Correction Method for Assessing Supraglacial Features on the Greenland Ice Sheet. *Frontiers in Remote Sensing*, *2*. https://doi.org/10.3389/frsen.2021.690474

Li, Y., Gao, H., Zhao, G., & Tseng, K.-H. (2020). A high-resolution bathymetry dataset for global reservoirs using multi-source satellite imagery and altimetry. *Remote Sensing of Environment*, *244*, 111831. https://doi.org/https://doi.org/10.1016/j.rse.2020.111831

Li, Y., Zhao, G., Allen, G. H., & Gao, H. (2023). Diminishing storage returns of reservoir construction. *Nature Communications*, *14*(1). https://doi.org/10.1038/s41467-023-38843-5

Li, Y., Zhao, G., Shah, D., Zhao, M., Sarkar, S., Devadiga, S., Zhao, B., Zhang, S., & Gao, H. (2021). NASA's MODIS/VIIRS Global Water Reservoir Product Suite

from Moderate Resolution Remote Sensing Data. *Remote Sensing*, *13*(4), 565. https://doi.org/10.3390/rs13040565

Ling, F., Li, X., Foody, G. M., Boyd, D., Ge, Y., Li, X., & Du, Y. (2020). Monitoring surface water area variations of reservoirs using daily MODIS images by exploring sub-pixel information. *ISPRS Journal of Photogrammetry and Remote Sensing*, *168*, 141–152. https://doi.org/https://doi.org/10.1016/j.isprsjprs.2020.08.008

McFeeters, S.K. (1996). The use of the Normalized Difference Water Index (NDWI) in the delineation of open water features. *International Journal of Remote Sensing, 17*, 1425-1432

McJannet, D. L., Webster, I. T., & Cook, F. J. (2012). An area-dependent wind function for estimating open water evaporation using land-based meteorological data. *Environmental Modelling and Software*, *31*. https://doi.org/10.1016/j.envsoft.2011.11.017

Mehran, A., Mazdiyasni, O., & AghaKouchak, A. (2015). A hybrid framework for assessing socioeconomic drought: Linking climate variability, local resilience, and demand. *Journal of Geophysical Research: Atmospheres*, *120*(15), 7520–7533. https://doi.org/https://doi.org/10.1002/2015JD023147

Meng, X., Liu, H., Du, Q., Xu, L., & Liu, Y. (2020). Evaluation of the performance of different methods for estimating evaporation over a highland open freshwater lake in mountainous area. *Water (Switzerland)*, *12*(12). https://doi.org/10.3390/w12123491

Messager, M. L., Lehner, B., Grill, G., Nedeva, I., & Schmitt, O. (2016). Estimating the volume and age of water stored in global lakes using a geo-statistical approach. *Nature Communications*, *7*. https://doi.org/10.1038/ncomms13603

Mhawej, M., Fadel, A., & Faour, G. (2020). Evaporation rates in a vital lake: a 34-year assessment for the Karaoun Lake. *International Journal of Remote Sensing*, *41*(14). https://doi.org/10.1080/01431161.2020.1739354

Moreo, M. T. (2015). *Evaporation data from Lake Mead and Lake Mohave, Nevada and Arizona, March 2010 through April 2015*.

Mu, Q., Zhao, M., & Running, S. W. (2011). Improvements to a MODIS global terrestrial evapotranspiration algorithm. *Remote Sensing of Environment*, *115*(8), 1781–1800. https://doi.org/10.1016/j.rse.2011.02.019

Murdock, H. E., Gibb, D., André, T., Appavou, F., Brown, A., Epp, B., Kondev, B., McCrone, A., Musolino, E., & Ranalder, L. (2019). *Renewables 2019 Global Status Report*.

Otsu, N. (1979). A Threshold Selection Method from Gray-Level Histograms. *IEEE Transactions on Systems, Man, and Cybernetics*, *9*(1), 62–66. https://doi.org/10.1109/TSMC.1979.4310076

Pekel, J. F., Cottam, A., Gorelick, N., & Belward, A. S. (2016). High-resolution mapping of global surface water and its long-term changes. *Nature*, *540*(7633). https://doi.org/10.1038/nature20584

Pinhassi, J., DeLong, E. F., Béjà, O., González, J. M., & Pedrós-Alió, C. (2016). Marine Bacterial and Archaeal Ion-Pumping Rhodopsins: Genetic Diversity, Physiology, and Ecology. *Microbiology and Molecular Biology Reviews*, *80*(4), 929–954. https://doi.org/10.1128/mmbr.00003-16

Plate, E. J. (2002). Flood risk and flood management. *Journal of Hydrology*, *267*(1–2). https://doi.org/10.1016/S0022-1694(02)00135-X

Rodell, M., Houser, P. R., Jambor, U., Gottschalck, J., Mitchell, K., Meng, C.-J., Arsenault, K., Cosgrove, B., Radakovich, J., Bosilovich, M., Entin, J. K., Walker, J. P., Lohmann, D., & Toll, D. (2004). The Global Land Data Assimilation System. *Bulletin of the American Meteorological Society*, *85*(3), 381–394. https://doi.org/https://doi.org/10.1175/BAMS-85-3-381

Schewe, J., Heinke, J., Gerten, D., Haddeland, I., Arnell, N. W., Clark, D. B., Dankers, R., Eisner, S., Fekete, B. M., Colón-González, F. J., Gosling, S. N., Kim, H., Liu, X., Masaki, Y., Portmann, F. T., Satoh, Y., Stacke, T., Tang, Q., Wada, Y., … Kabat, P. (2014). Multimodel assessment of water scarcity under climate change. *Proceedings of the National Academy of Sciences of the United States of America*, *111*(9). https://doi.org/10.1073/pnas.1222460110

Schwab, D. J., & Morton, J. A. (1984). Estimation of Overlake Wind Speed from Overland Wind Speed: A Comparison of Three Methods. *Journal of Great Lakes Research*, *10*(1). https://doi.org/10.1016/S0380-1330(84)71808-9

Schwatke, C., Dettmering, D., Bosch, W., & Seitz, F. (2015). DAHITI - An innovative approach for estimating water level time series over inland waters using multi-mission satellite altimetry. *Hydrology and Earth System Sciences*, *19*(10). https://doi.org/10.5194/hess-19-4345-2015

Shah, D., Zhang, S., Sarkar, S., Davidson, C., Zhang, R., Zhao, M., Devagida, S., Román, M., Gao, H., (Under Review). Transitioning from NASA's MODIS to VIIRS Global Water Reservoir (GWR) Products: A Perspective of Continuity, Nature Scientific Data.

Veldkamp, T. I. E., Wada, Y., Aerts, J. C. J. H., Döll, P., Gosling, S. N., Liu, J., Masaki, Y., Oki, T., Ostberg, S., Pokhrel, Y., Satoh, Y., Kim, H., & Ward, P. J. (2017). Water scarcity hotspots travel downstream due to human interventions in the 20th and 21st century. *Nature Communications*, *8*(1), 15697. https://doi.org/10.1038/ncomms15697

Vermote, E., Franch, B., & Claverie, M. (2016). VIIRS/NPP Surface Reflectance 8-Day L3 Global 500m SIN Grid V001. *NASA EOSDIS Land Process. DAAC*.

Yao, F., Livneh, B., Rajagopalan, B., Wang, J., Crétaux, J. F., Wada, Y., & Berge-Nguyen, M. (2023). Satellites reveal widespread decline in global lake water storage. *Science*, *380*(6646). https://doi.org/10.1126/SCIENCE.ABO2812

Yao, F., Wang, J., Wang, C., & Crétaux, J.-F. (2019). Constructing long-term high-frequency time series of global lake and reservoir areas using Landsat imagery. *Remote Sensing of Environment*, *232*, 111210. https://doi.org/https://doi.org/10.1016/j.rse.2019.111210

Yigzaw, W., Li, H.-Y., Demissie, Y., Hejazi, M. I., Leung, L. R., Voisin, N., & Payn, R. (2018). A New Global Storage-Area-Depth Data Set for Modeling Reservoirs in Land Surface and Earth System Models. *Water Resources Research*, *54*(12), 10, 310–372, 386. https://doi.org/https://doi.org/10.1029/2017WR022040

Zhang, H., Gorelick, S. M., Zimba, P. V., & Zhang, X. (2017). A remote sensing method for estimating regional reservoir area and evaporative loss. *Journal of Hydrology*, *555*. https://doi.org/10.1016/j.jhydrol.2017.10.007

Zhang, S., Gao, H., & Naz, B. S. (2014). Monitoring reservoir storage in South Asia from multisatellite remote sensing. *Water Resources Research*, *50*(11). https://doi.org/10.1002/2014WR015829

Zhao, G., & Gao, H. (2018). Automatic Correction of Contaminated Images for Assessment of Reservoir Surface Area Dynamics. *Geophysical Research Letters*, *45*(12). https://doi.org/10.1029/2018GL078343

Zhao, G., & Gao, H. (2019). Estimating reservoir evaporation losses for the United States: Fusing remote sensing and modeling approaches. *Remote Sensing of Environment*, *226*. https://doi.org/10.1016/j.rse.2019.03.015

Zhao, G., Gao, H., & Cai, X. (2020). Estimating lake temperature profile and evaporation losses by leveraging MODIS LST data. *Remote Sensing of Environment*, *251*, 112104. https://doi.org/https://doi.org/10.1016/j.rse.2020.112104

Zhao, G., Li, Y., Zhang, S., Shah, D., & Gao, H. (2021). *Collection 6.1 MODIS Global Reservoir Product Algorithm Theoretical Basis Document (ATBD)*.

Zhao, G., Li, Y., Zhou, L., & Gao, H. (2022). Evaporative water loss of 1.42 million global lakes. *Nature Communications*, *13*(1), 3686. https://doi.org/10.1038/s41467-022-31125-6

Zhou, T., Nijssen, B., Gao, H., & Lettenmaier, D. P. (2016). The Contribution of Reservoirs to Global Land Surface Water Storage Variations. *Journal of Hydrometeorology*, *17*(1), 309–325. https://doi.org/https://doi.org/10.1175/JHM-D-15-0002.1

Zhou, Y. (2020). Exploring multidecadal changes in climate and reservoir storage for assessing nonstationarity in flood peaks and risks worldwide by an integrated frequency analysis approach. *Water Research*, *185*, 116265. https://doi.org/https://doi.org/10.1016/j.watres.2020.116265

Appendix-A

Table A1. List of the 164 reservoirs and their attributes

ID	GRAND_ID	Hylak_id	Res_name	Country	Continent	a,b	storage new	area new	elevation new	Capacity_source	lon,lat
1	5058	11	Baikal	Russia	Asia	0.00447, 312.77026	23615.39	32265.61	456.88	GRanD	104.32, 52.24
2	3667	156	Volta	Ghana	Africa	0.00365, 55.58562	148	8502	86.65	wikipedia	0.06, 6.3
3	4478	152	Nasser	Egypt	Africa	0.00469, 152.81994	162	6500	183.28	literature	32.89, 23.97
4	4056	172	Kariba Reservoir	Zambia	Africa	0.01119, 424.98467	180	5400	485.41	wikipedia	28.76, -16.52
5	5055	110	Bratsk Reservoir	Russia	Asia	0.00657, 367.92163	169.27	5470	403.85	wikipedia	101.78, 56.29
6	4787	122	Zaysan	Kazakhstan	Asia	0.00465, 370.20585	49.8	5490	395.74	GRanD	83.35, 49.66
7	2294	73	Guri Reservoir	Venezuela	South America	0.0144, 217.16716	135	4250	278.38	wikipedia	-63, 7.77
8	1995	43	Caniapiscau Reservoir	Canada	North America	0.01218, 488.99841	53.79	4275	541.08	GRanD	-69.78, 54.85
9	1394	46	Robert Bourassa Reservoir	Canada	North America	0.0111, 143.99061	61.7	2905	176.24	Hydro-Québec	-77.45, 53.79
10	2516	77	Sobradinho Reservoir	Brazil	South America	0.00571, 375.26816	34.1	3017.9	392.5	GRanD	-40.82, -9.42
11	712	51	Cedar	Canada	North America	0.00217, 250.49224	9.64	2668.46	256.29	GRanD	-99.29, 53.16
12	1396	47	La Grande 3 Reservoir	Canada	North America	0.02539, 195.25843	60	2451	257.48	Hydro-Québec	-75.96, 53.73

13	2365	76	Tucurui Reservoir	Brazil	South America	0.01322, 40.95573	45.5	2606	75.4	GRanD	-49.65, -3.83
14	4375	128	Tsimlyanskoye Reservoir	Russia	Euro	0.01177, 7.63989	23.86	2702	39.44	literature	42.11, 47.61
15	5834	115	Zeyskoye Reservoir	Russia	Asia	0.02065, 266.43675	68.4	2420	316.41	wikipedia	127.31, 53.77
16	5180	96	Vilyuy Reservoir	Russia	Asia	0.02852, 182.74156	35.9	2170	244.62	wikipedia	112.48, 63.03
17	4783	93	Khantayskoye Reservoir	Russia	Asia	0.00445, 49.76375	23.5	2221 .61	59.64	GRanD	87.81, 68.16
18	4505	171	Cahora Bassa Reservoir	Mozambique	Africa	0.01542, 286.9568	55.8	2739	329.18	wikipedia	32.7, -15.58
19	6	40	Williston	Canada	North America	0.0529, 580.99344	39.47	1773	674.79	literature	-122.2, 56.02
20	4472	144	Buhayrat ath Tharthar	Iraq	Asia	0.03955, -19.46261	85.59	2135 .54	65	literature	43.46, 33.69
21	5056	112	Krasnoyarsk Reservoir	Russia	Asia	0.03863, 162.77316	73.3	2000	240.04	wikipedia	92.29, 55.93
22	4623	106	Kama Reservoir	Russia	Euro	0.00744, 96.07894	12.2	1915	110.32	wikipedia	56.34, 58.12
23	1957	69	Okeechobee	United States of America	North America	0.00617, -5.57499	3.546	1536 .8	3.9	wikipedia	-81.1, 26.94
24	5295	145	Hungtze	China	Asia	0.00749, 1.45816	13.5	2074 .61	17	literature	118.73, 33.09
25	4474	146	Razazah	Iraq	Asia	0.01457, 11.06852	25.75	1621	34.69	literature	43.89, 32.7
26	2023	60	Gouin Reservoir	Canada	North America	0.00068, 402.90611	8.57	1570	403.98	GRanD	-74.1, 48.36
27	4789	135	Qapshaghay Bogeni Reservoir	Kazakhstan	Asia	0.00897, 467.10974	28.1	1850	483.71	GRanD	77.1, 43.92
28	753	62	Fort Berthold Reservoir	United States of America	North America	0.02467, 528.64792	29.38	1477 .4	565.1	wikipedia	-101.43, 47.51

29	2445	83	Aperea Reservoir	Paraguay	South America	0.02242, 48.84199	21	1600	84.71	literature	-56.63, -27.39
30	870	65	Oahe	United States of America	North America	0.02172, 462.72715	28.35	1429.57	493.78	wikipedia	-100.4, 44.46
31	2390	80	Ilha Solteira Reservoir	Brazil	South America	0.03237, 290.94542	21.17	1200	329.78	GRanD	-51.38, -20.37
32	4629	118	Saratov Reservoir	Russia	Euro	0.02563, -0.27741	12.9	1117.7	28.36	GRanD	47.76, 52.05
33	4350	94	Imandra	Russia	Euro	0.18726, -62.86735	10.8	1062.37	136.07	GRanD	32.55, 67.41
34	3640	155	Kainji Reservoir	Nigeria	Africa	0.03997, 93.99579	15	1071.23	136.81	wikipedia	4.61, 9.87
35	4785	113	Novosibirskoye	Russia	Asia	0.01419, 98.78019	8.8	1070	113.97	wikipedia	83, 54.84
36	4625	111	Cheboksary	Russia	Euro	0.02447, 39.29789	13.85	1080.38	65.73	literature	47.46, 56.14
37	4359	1163	Ilmen	Russia	Euro	0.0083, 9.98411	12	1120	19.28	wikipedia	31.28, 58.46
38	4480	1527	Jebel Aulia Reservoir	Sudan	Africa	0.00624, 375.01032	3.5	861.19	380.39	FAO	32.48, 15.24
39	1397	623	Opinaca Reservoir	Canada	North America	0.02118, 194.07727	8.5	1040	216.1	wikipedia	-76.58, 52.21
40	2392	943	Furnas	Brazil	South America	0.0437, 720.07262	22.59	1127.07	769.32	wikipedia	-46.31, -20.67
41	2368	922	Serra da Mesa Reservoir	Brazil	South America	0.03356, 410.19963	54.4	1784	470.07	wikipedia	-48.3, -13.84
42	4624	1169	Votkinsk Reservoir	Russia	Euro	0.03892, 53.1356	9.4	850.82	86.25	wikipedia	54.08, 56.8
43	6201	1632	Argyle Reservoir	Australia	Oceania	0.02806, 66.43617	10.76	981.21	93.97	wikipedia	128.74, -16.12
44	731	710	Rainy	Canada	North America	0.00078, 336.08674	0.69	829.45	336.73	GRanD	-93.36, 48.62

45	307	721	Fort Peck	United States of America	North America	0.04376, 643.31691	22.77	969.86	685.76	wikipedia	-106.41, 48
46	2375	928	Tres Marias Reservoir	Brazil	South America	0.03553, 539.11233	21	1040	576.06	wikipedia	-45.27, -18.21
47	2012	697	Pipmuacan Reservoir	Canada	North America	0.0498, 360.46403	13.9	978	409.16	wikipedia	-69.77, 49.36
48	4679	1307	Chardarinskoye	Kazakhstan	Asia	0.01786, 238.24413	5.7	800.66	252.54	wikipedia	67.96, 41.25
49	4626	1175	Nizhnekamsk Reservoir	Russia	Euro	0.0138, 50.37324	13.8	1084	65.34	wikipedia	52.28, 55.7
50	2456	966	Negro Reservoir	Uruguay	South America	0.0194, 62.00777	8.8	1070	82.77	wikipedia	-56.42, -32.83
51	2343	981	Chocon Reservoir	Argentina	South America	0.01519, 365.74893	22	820	378.2	GRanD	-68.76, -39.27
52	4442	1348	Ataturk Dam	Turkey	Asia	0.10643, 454.25042	48.7	817	541.2	GRanD	38.32, 37.49
53	2513	915	Itaparica Reservoir	Brazil	South America	0.03337, 279.33376	10.7	781.21	305.4	wikipedia	-38.31, -9.14
54	4464	1365	Assad	Syria	Asia	0.05942, 266.62629	11.7	610	302.87	wikipedia	38.55, 35.86
55	3650	1558	Lagdo Reservoir	Cameroon	Africa	0.0374, 190.15542	7.7	691.12	216	FAO	13.69, 9.06
56	1269	838	Toledo Bend Reservoir	United States of America	North America	0.02039, 39.45546	5.52	636.18	52.43	wikipedia	-93.57, 31.18
57	6922	624	Eastmain Reservoir	Canada	North America	0.06785, 245.91598	6.94	602.9	286.82	literature	-75.89, 52.19
58	2009	688	Outardes 4 Reservoir	Canada	North America	0.19049, 239.61011	24.5	640	361.53	Hydro-Québec	-68.91, 49.71
59	4349	1036	Kovdozero	Russia	Euro	0.00193, 78.17686	11.52	745	79.62	GRanD	31.76, 68.6
60	2380	931	Sao Simao Reservoir	Brazil	South America	0.0523, 369.16877	12.5	703	405.94	wikipedia	-50.5, -19.02

61	610	809	Mead	United States of America	North America	0.13619, 288.76038	34.07	659.3	374.6	USBR	-114.73, 36.02
62	5087	1473	Yamdrok	China	Asia	0.01275, 4435.35521	14.6	638	4443.49	literature	90.38, 29.1
63	1391	866	Angostura Reservoir	Mexico	North America	0.08079, 478.95889	18.2	640	530.67	wikipedia	-92.78, 16.4
64	4991	1524	Srisailam Reservoir	India	Asia	0.03079, 253.3044	8.29	534.05	269.75	CWC	78.9, 16.09
65	2455	964	Grande Reservoir	Argentina	South America	0.03068, 16.88963	5	592.83	35.08	wikipedia	-57.94, -31.27
66	4843	1484	Gandhisagar Reservoir	India	Asia	0.03366, 379.03449	6.83	619.89	399.9	CWC	75.55, 24.7
67	2397	946	Promissao Reservoir	Brazil	South America	0.08038, 342.73167	7.41	513.39	384	GRanD	-49.78, -21.3
68	282	698	Arrow	Canada	North America	0.17477, 351.0668	10.3	504.82	439.3	USACE	-117.78, 49.34
69	2382	934	Agua Vermelha Reservoir	Brazil	South America	0.05626, 351.61681	11.03	563.15	383.3	wikipedia	-50.35, -19.87
70	4898	1502	Hirakud Reservoir	India	Asia	0.02204, 177.26302	5.38	669.62	192.02	CWC	83.85, 21.52
71	3041	1568	Kossour Reservoir	Ivory Coast	Africa	0.03423, 169.77945	27.68	1058.2	206	GRanD	-5.47, 7.03
72	4784	1058	Kureiskaya	Russia	Asia	0.04971, 67.89284	9.96	558	95.63	literature	88.29, 66.95
73	3071	1104	Storsjon	Sweden	Euro	0.00422, 291.0872	0.5	484.6	293.13	GRanD	14.47, 63.3
74	316	730	Flathead Lake	United States of America	North America	0.13239, 816.09051	23.2	510	883.61	wikipedia	-114.23, 47.68
75	2004	661	Kempt	Canada	North America	0.03312, 478.60112	2.22	470.44	494.18	GRanD	-70.53, 50.66
76	6700	1123	Kolyma dam	Russia	Asia	0.13658, 390.9085	15.08	454.6	453	wikipedia	150.23, 62.05

77	4501	1612	Mtera Reservoir	United Republic of Tanzania	Africa	0.02183, 688.04662	3.2	478.83	698.5	literature	35.98, -7.14
78	4686	1320	Kayrakkumskoye	Tajikistan	Asia	0.02143, 335.23897	4.2	513	346.23	wikipedia	69.82, 40.28
79	250	628	Kinbasket	Canada	North America	0.31717, 622.76738	24.76	430	759.15	wikipedia	-118.57, 52.08
80	4634	1313	Mingechaurskoye	Azerbaijan	Asia	0.07215, 42.01887	15.73	567.97	83	wikipedia	47.03, 40.8
81	2431	956	Lago del Río Yguazú	Paraguay	South America	0.04517, 203.13232	8.47	620	231.14	wikipedia	-54.97, -25.37
82	4858	1487	Govind Ballabah Pant	India	Asia	0.06208, 241.75327	5.65	426.36	268.22	CWC	83, 24.2
83	4422	1332	Keban Baraji	Turkey	Asia	0.11302, 772.50564	30.6	675	848.79	wikipedia	38.76, 38.81
84	2340	978	Los Barreales	Argentina	South America	0.30759, 290.07305	27.7	413	417.11	literature	-68.69, -38.58
85	4859	1488	Bansagar Lake	India	Asia	0.05088, 317.64432	5.17	471.6	341.64	CWC	81.29, 24.19
86	1275	839	Sam Rayburn Reservoir	United States of America	North America	0.0355, 35.65711	3.55	455.64	50.11	TWDB	-94.11, 31.07
87	2414	953	Barra Bonita	Brazil	South America	0.00228, 565.24837	7.01	542	566.48	GRanD	-49.23, -23.21
88	4739	1504	Ukal	India	Asia	0.04229, 83.59772	6.62	509.85	105.16	CWC	73.6, 21.26
89	479	788	Utah Lake	United States of America	North America	0.02307, 1359.51211	1.07	380	1368.28	wikipedia	-111.89, 40.36
90	305	719	Pend Oreille Lake	United States of America	North America	0.22845, 541.65792	54.2	381.47	628.8	wikipedia	-117, 48.18
91	4994	1526	Tungabhadra	India	Asia	0.04122, 483.33699	3.28	349.42	497.74	CWC	76.33, 15.27
92	4461	1355	Mosul Dam Lake	Iraq	Asia	0.16032, 273.38375	11.1	353.16	330	wikipedia	42.83, 36.63

93	4470	1392	Habbaniyah	Iraq	Asia	0.07125, 114.61642	8.2	418.4	144.43	literature	42.35, 34.21
94	4946	1509	Sriramsagar Reservoir	India	Asia	0.04005, 319.94975	2.3	314.38	332.54	CWC	78.34, 18.97
95	2376	929	Lago das Brisas	Brazil	South America	0.08818, 471.03368	17	559.6	520.38	wikipedia	-49.1, -18.41
96	2356	720	Meelpaeg	Canada	North America	0.0041, 269.35893	2.16	314.9	270.65	GRanD	-56.78, 48.17
97	4260	1678	Hendrik Verwoerd	South Africa	Africa	0.06907, 1236.10289	5.34	374	1261.93	wikipedia	25.5, -30.62
98	1387	864	Malpaso	Mexico	North America	0.30032, 89.06386	9.17	309.45	182	literature	-93.6, 17.18
99	1379	861	Inhernillo	Mexico	North America	0.14118, 116.65544	12	400	173.13	wikipedia	-101.89, 18.27
100	4184	1657	Vaaldam	South Africa	Africa	0.0358, 1472.81742	2.61	320	1484.27	wikipedia	28.12, -26.88
101	5062	1358	Longyangxia	China	Asia	0.18321, 2518.97907	24.7	383	2589.15	wikipedia	100.92, 36.12
102	3727	1111	Hoytiainen	Finland	Euro	0.0064, 86.17122	2.39	293	88.05	GRanD	29.48, 62.83
103	1423	741	Baskatong	Canada	North America	0.05663, 207.28526	2.63	280	223.14	GRanD	-75.98, 46.72
104	5803	1549	Tri An Lake	Vietnam	Asia	0.07216, 39.48203	2.76	323	62.79	wikipedia	107.04, 11.11
105	2007	680	Peribonka	Canada	North America	0.10611, 411.5385	5.18	270.72	440.26	GRanD	-71.25, 49.9
106	4942	1507	Jayakwadi	India	Asia	0.03201, 451.67121	2.17	382.39	463.91	CWC	75.37, 19.49
107	3638	1554	Shiroro	Nigeria	Africa	0.08602, 350.89662	7	312	377.73	FAO	6.84, 9.97
108	4379	1289	Tshchikskoye	Russia	Euro	0.06161, 16.03972	3.05	286.28	33.68	FAO	39.12, 44.99

109	710	589	Tobin	Canada	North America	0.00897, 311.22766	2.2	263.86	313.59	GRanD	-103.4, 53.66
110	5796	1528	Noi	Thailand	Asia	0.05709, 129.50217	1.97	288	145.94	wikipedia	105.43, 15.21
111	4483	1543	Roseires Reservoir	Sudan	Africa	0.02506, 475.84407	7.4	450	487.12	wikipedia	34.39, 11.8
112	4675	1306	Toktogul'skoye	Kyrgyzstan	Asia	0.55471, 743.53409	19.5	284.3	901.24	wikipedia	72.65, 41.68
113	6698	1700	Gordon	Australia	Oceania	0.37007, 208.53588	12.4	278	311.42	wikipedia	145.98, -42.73
114	4964	1513	Ujani	India	Asia	0.05453, 482.16622	1.52	268.91	496.83	CWC	75.12, 18.07
115	2312	959	Hondo	Argentina	South America	0.02922, 266.72004	1.74	330	276.36	WLDB	-64.89, -27.52
116	4362	1171	Ivankovo Reservoir	Russia	Euro	0.01794, 119.50914	1.17	220.57	123.47	GRanD	37.12, 56.73
117	4702	1398	Tarbela	Pakistan	Asia	0.52839, 351.45663	13.69	250	483.55	wikipedia	72.69, 34.09
118	4985	1519	Nagarjuna	India	Asia	0.29044, 100.77784	6.84	272.18	179.83	wikipedia	79.31, 16.57
119	3070	1102	Kallsjon	Sweden	Euro	0.02782, 387.52135	0.45	189.74	392.8	GRanD	13.34, 63.43
120	4431	1337	Karakaya	Turkey	Asia	0.22073, 631.76449	9.5	298	697.54	wikipedia	39.14, 38.23
121	4792	1423	Beas	India	Asia	0.20473, 371.49329	6.16	254.85	423.67	CWC	75.95, 31.97
122	4047	1622	Tshangalele	Democratic Republic of the Congo	Africa	0.03102, 1119.03312	1.267	225.65	1126.03	GRanD	27.24, -10.75
123	4485	1555	Finchaa	Ethiopia	Africa	0.01891, 2216.55235	0.65	196.13	2220.26	FAO	37.36, 9.56

124	4989	1521	Almatti	India	Asia	0.05275, 504.12335	3.11	293.42	519.6	CWC	75.89, 16.33
125	4707	1408	Mangla	Pakistan	Asia	0.20109, 320.1312	9.12	251	370.6	wikipedia	73.64, 33.15
126	4836	1481	Rana Pratap	India	Asia	0.1391, 324.74	1.44	197.66	352.81	CWC	75.58, 24.92
127	3014	1545	Bagre	Burkina Faso	Africa	0.05719, 223.53693	1.7	255	238.12	literature	-0.55, 11.47
128	1991	916	Junin	Peru	South America	0.02312, 4079.83703	1.08	206.71	4084.62	WLDB	-76.19, -10.98
129	4881	1496	Bargi Dam Reservoir	India	Asia	0.08518, 401.51078	3.18	236.24	422.76	CWC	79.93, 22.95
130	6686	1699	Great Lake	Australia	Oceania	0.40346, 969.53157	3.36	176	1040.54	GRanD	146.73, -41.98
131	6800	1704	Hawea	New Zealand	Oceania	0.14631, 323.54085	2.18	150	345.49	GRanD	169.25, -44.61
132	3676	1619	Albufeira da Quiminha	Angola	Africa	0.13121, 34.99206	1.56	129.05	51.93	GRanD	13.79, -8.96
133	6629	1695	Eucumbene	Australia	Oceania	0.46484, 1097.64507	4.8	145.42	1165.24	wikipedia	148.62, -36.13
134	1320	855	Falcon Reservoir	United States of America	North America	0.06972, 71.73912	3.88	311.84	93.48	TWDB	-99.17, 26.56
135	597	802	Lake Powell	United States of America	North America	0.1406, 1047.2	30	609.38	1127.76	wikipedia	-111.49, 36.94
136	4463	1362	Dukan	Iraq	Asia	0.18893, 462.6788	6.97	270	513.69	wikipedia	44.96, 35.96
137	1230	835	Cedar Creek Reservoir	United States of America	North America	0.09423, 85.91971	0.8	133.03	98.15	TWDB	-96.07, 32.18
138	4041	1551	Lake Maga	Cameroon	Africa	0.01933, 309.62551	0.68	148.72	312.5	literature	15.05, 10.83
139	5157	1530	Pasak Chonlasit	Thailand	Asia	0.05295, 33.58769	0.79	158.87	42	literature	101.08, 14.85

140	6594	1650	Fairbairn	Australia	Oceania	0.13, 186.48395	2.29	179.43	209.81	wikipedia	148.06, -23.65
141	6628	1694	Hume	Australia	Oceania	0.15399, 161.81633	3.04	201.9	192	wikipedia	147.03, -36.11
142	4500	1605	Kikuletwa	United Republic of Tanzania	Africa	0.1, 677.01366	0.6	126.33	689.65	wikipedia	37.47, -3.82
143	4958	1511	Nizam sagar	India	Asia	0.0893, 419.95709	0.5	92.75	428.24	CWC	77.93, 18.2
144	6606	1690	Victoria	Australia	Oceania	0.16558, 7.52685	0.68	122	27.73	GRanD	141.28, -34.04
145	1869	826	Grenada Lake	United States of America	North America	0.12614, 49.34905	1.54	128.29	65.53	Lakes Online	-89.77, 33.82
146	138	790	Canyon	United States of America	North America	0.68749, 1300.93547	1.61	108.39	1373.12	wikipedia	-121.09, 40.18
147	4638	1329	Aras Dam Lake	Azerbaijan	Asia	0.11845, 762.76554	1.35	145	779.94	wikipedia	45.4, 39.09
148	4481	1529	Khashm el-Girba	Sudan	Africa	0.09342, 463.08227	1.3	125	474.76	wikipedia	35.9, 14.93
149	370	8978	Lake Cascade	United States of America	North America	0.16232, 1455.02068	0.85	101.98	1471.57	wikipedia	-116.05, 44.52
150	3695	11663	Seitevare	Sweden	Euro	0.62918, 419.1852	1.68	81	470.15	GRanD	18.57, 66.97
151	4484	15827	Yardi	Ethiopia	Africa	0.33044, 533.59442	2.32	104.87	568.25	GRanD	40.54, 10.23
152	119	9138	Clear Lake Reservoir	United States of America	North America	0.19968, 1345.80215	0.65	100.36	1365.84	wikipedia	-121.08, 41.93
153	5196	14551	Guanting Shuiku	China	Asia	0.10764, 465.09336	4.16	130	479.09	GRanD	115.6, 40.23
154	2953	15102	Barrage Al Massira	Morocco	Africa	0.33916, 241.40761	2.76	80	268.54	wikipedia	-7.64, 32.47
155	1319	9634	Venustiano Carranza	Mexico	North America	0.09456, 252.29236	1.31	150.56	266.53	literature	-100.62, 27.51

156	4471	15001	Lake Hamrin	Iraq	Asia	0.11963, 80.22516	4.61	228	107.5	literature	44.97, 34.12
157	4826	15490	Matatila	India	Asia	0.10028, 297.22136	0.71	112.07	308.46	CWC	78.37, 25.1
158	1263	9503	Twin Buttes	United States of America	North America	0.49517, 576.78181	0.23	29.47	591.37	TWDB	-100.52, 31.37
159	4997	15748	Somasila	India	Asia	0.17144, 74.32045	1.99	153.17	100.58	CWC	79.3, 14.49
160	5183	14389	Hongshan Reservoir	China	Asia	0.23268, 422.07692	2.56	66.9	437.64	GRanD	119.7, 42.75
161	6583	16242	Lake Ross	Australia	Oceania	0.11178, 32.60497	0.417	82	41.77	wikipedia	146.74, -19.41
162	4978	15697	Yeleru Reservoir	India	Asia	0.58856, 57.51076	0.51	49.36	86.56	CWC	82.08, 17.3
163	4696	14730	South Surkhan Reservoir	Uzbekistan	Asia	0.33795, 397.79868	0.8	40.26	411.41	GRanD	67.63, 37.83
164	5287	15019	Zhaopingtai Reservoir	China	Asia	0.35804, 157.62551	0.71	46.5	174.27	GRanD	112.77, 33.73

*The 164 reservoirs include 13 regulated natural lakes, whose IDs are 1, 6, 20, 23, 33, 37, 44, 62, 73, 102, 131, 150, and 151.

[1]*a* and *b* are the coefficients used in the A-E relationship equation: h=a*A + b, where h and A are elevation (m) and area (km^2), respectively.

Vc, *Ac*, and *Ec* represent storage, area, and elevation values at capacity, respectively.